Elastic least-squares reverse time migration

Yuting Duan, Paul Sava, and Antoine Guitton
Center for Wave Phenomena, Colorado School of Mines

ABSTRACT
Least-squares migration (LSM) can produce images with improved resolution and reduced migration artifacts. We propose a method for elastic least-squares reverse time migration (LSRTM) based on different types of imaging condition. Perturbation imaging condition leads to images for squared P and S velocity models; the displacement imaging condition crosscorrelates components of the source and receiver displacement wavefields; the potential and scalar imaging conditions lead to images of various combination of P- and S-wave modes. Using each imaging condition, we form an LSM algorithm by defining the migration and demigration operators. Among the combined images, the perturbation and scalar images do not suffer from polarity changes, and thus they can be stacked over experiments without an additional polarity correction. The scalar imaging condition requires geologic dip information, while the perturbation imaging condition does not need additional information. Therefore, we apply LSRTM using the perturbation imaging condition to 2D examples. Results show that elastic LSRTM iteratively increases the image resolution and attenuates artifacts. Also, the computed LSRTM images have correct relative-amplitudes, which are suitable for reservoir characterization.

Key words: elastic imaging, least-squares migration

1 INTRODUCTION

Seismic migration is a technique for obtaining structural images of the subsurface from recorded seismic data. Starting from a linearized forward operator derived based on assumptions about the wave equation and model parameters, seismic migration can be formulated as the adjoint operator that maps seismic data to a subsurface image (Claerbout, 1992). Migration images not only can show geologic structures, but can also provide information about material properties, such as reflectivity, that are important for reservoir characterization. In practice, however, migration images often contain various undesirable artifacts. One reason for these artifacts is that the estimated models of the subsurface properties needed for wavefield reconstruction are not of sufficient accuracy. Also, the quality of migration images degrades due to insufficient data resulting from, for example, limited bandwidth and limited acquisition coverage. Finally, migration images are usually computed under assumptions about wave propagation in the subsurface, e.g., that the earth is isotropic and acoustic, that are, to varying degrees, inaccurate. Taken together, these limitations and assumptions result in artifacts and images with poor resolution.

Advances in seismic acquisition and ongoing improvements in computational capability have made imaging using elastic waves increasingly feasible (Sun et al., 2006; Yan and Sava, 2008; Denli and Huang, 2008; Artman et al., 2009; Wu et al., 2010; Du et al., 2012; Duan and Sava, 2015; Rocha et al., 2015). Compared to acoustic images, elastic images can provide more information about the subsurface. For example, they can provide information about fracture distributions and elastic properties. However, elastic migration also suffers from issues that negatively affect the quality of the images. Nonphysical modes are one source of artifacts in elastic images (Duan and Sava, 2014). These nonphysical modes result from arrivals in the recorded data that cannot be separated by wave mode, and as a result are migrated using an incorrect model of wave propagation velocity. Such nonphysical modes lead to energy spreading to incorrect locations, thus generating artifacts in the image.

Least-squares migration (LSM) is an improved imaging algorithm that reduces these migration artifacts and also improves the resolution of migration images. LSM is a linearized waveform inversion that seeks to find the image that best predicts, in a least-squares sense, the recorded seismic data (Schuster, 1993; Nemeth et al., 1999; Dai et al., 2011). Schuster (1993) proposes LSM for cross-well data while Nemeth et al. (1999) apply this technique to surface data. Their studies show that LSM can significantly improve the spatial resolution of the images, and can also reduce migration artifacts arising from limited aperture, coarse sampling, and acquisition gaps.

LSM can be implemented using a Kirchkoff engine

(Nemeth et al., 1999; Dai et al., 2011), one-way wave equation (Kuehl and Sacchi, 2002; Kaplan et al., 2010; Huang and Schuster, 2012), or two-way wave equation, i.e., least squares reverse-time migration (LSRTM) (Dai and Schuster, 2013; Dong et al., 2012; Luo and Hale, 2014; Wong et al., 2015). For elastic LSM, Stanton and Sacchi (2015) propose elastic least-squares migration using a one-way wave equation, and they compute PP and PS images from two-component elastic data in isotropic media. Although computationally expensive, RTM is advantageous for velocity models with complicated geologic structures that result in wavefield multi-pathing.

In this paper we propose four elastic LSRTM algorithms based on different imaging conditions. We derive a new perturbation imaging condition for squared P and S velocity models. We also show an LSRTM algorithm using the displacement imaging condition crosscorrelating each component of the source and receiver displacement wavefields. Finally we derive LSRTM algorithms using the potential and scalar elastic imaging conditions, which provide images for different combinations of P and S modes. The PS and SP images computed using the potential imaging condition are vectors, while those computed using the scalar imaging condition are scalars. Among the four types of images, the perturbation image and scalar image do not suffer from polarity changes, and they can be stacked over experiments without an additional polarity correction. Compared to the scalar imaging condition, which requires the local reflector normal vector as an input, the perturbation imaging condition does not need additional information about the subsurface. Using the perturbation imaging condition, we demonstrate that we are able to obtain images with higher resolution and reduced migration artifacts, including those caused by nonphysical modes.

2 THEORY

LSM aims to find the image that best predicts, in a least-squares sense, the recorded seismic data. For elastic migration, we consider a vector image $\mathbf{m}$ which contains both compressional and shear wave lithological information. We treat migration as an adjoint operator $\mathbf{F}^{\mathsf{T}}$ that transforms recorded data $\mathbf{d}$ to image $\mathbf{m}$, and thus the forward process can be expressed as

$$\mathbf{F}\mathbf{m} = \mathbf{d}\ , \tag{1}$$

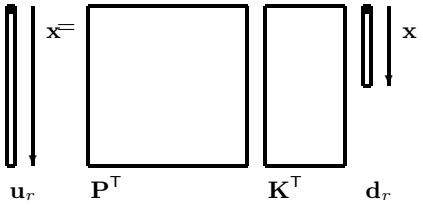
where $\mathbf{F}$ is the demigration operator.

For LSM, one typically updates the model iteratively by minimizing the objective function

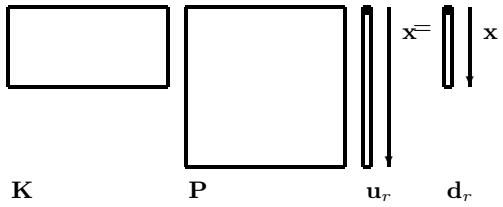
$$\mathcal{J} = \sum_{e} \frac{1}{2} \| \mathbf{W}\left(\mathbf{F}\mathbf{m} - \mathbf{d}_r\right) \|^2\ , \tag{2}$$

which evaluates the misfit between observed data $\mathbf{d}_r\left(e, \mathbf{x}, t\right)$ and predicted data $\mathbf{F}\mathbf{m}$ for each experiment e. Matrix $\mathbf{W}\left(e, \mathbf{x}, t\right)$ denotes the data weighting operator, which can be applied for various purposes. For example, Trad (2015) use matrix $\mathbf{W}$ to eliminate the impact of high-amplitude noise or missing traces on inversion; Wong et al. (2015) use matrix $\mathbf{W}$ to down-weight the salt reflection energy. In this paper, we use the data weighting term to balance the amplitudes of all arrivals in the recorded data.

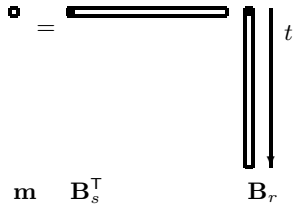
Given an imaging condition, we can define the migration and demigration operators $\mathbf{F}^{\mathsf{T}}$ and $\mathbf{F}$, respectively. For algorithms based on different imaging conditions, we need to construct the source and receiver displacement wavefields, $\mathbf{u}_s$ and $\mathbf{u}_r$, and use the displacement wavefields to compute matrices $\mathbf{B}_s$ and $\mathbf{B}_r$. The operation that transforms recorded data $\mathbf{d}_r$ to source displacement wavefield $\mathbf{u}_r$ can be represented as



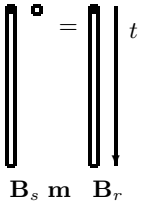
where operator $\mathbf{K}^{\mathsf{T}}$ injects the recorded data $\mathbf{d}_r$ to the wavefield at the receiver locations. The adjoint wave propagation operator $\mathbf{P}^{\mathsf{T}}$ back propagates the recorded data into the receiver wavefield $\mathbf{u}_r$. The shape of the boxes indicates the size of the matrices and vectors. The vertical axis depicts space, s.t., every cell (highlighted in black) of the vectors $\mathbf{u}_r$ and $\mathbf{d}_r$ contains the wavefield or the data for all time samples at one spatial location. The operator that maps wavefield $\mathbf{u}_r$ to data $\mathbf{d}_r$ is $\mathbf{K}\mathbf{P}$. Operator $\mathbf{P}$ forward propagates the wavefield $\mathbf{u}_r$, and then operator $\mathbf{K}$ extracts the data $\mathbf{d}_r$ at receiver locations:



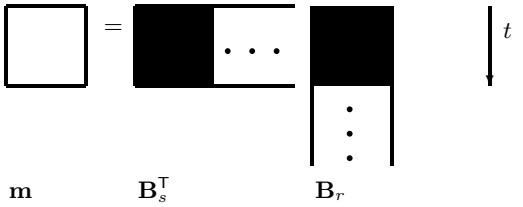
For migration, we crosscorrelate the constructed source and receiver wavefields, $\mathbf{B}_s$ and $\mathbf{B}_r$, respectively. By zooming into one spatial sample of the wavefield vector shown above, each sample is a vector as a function of time t, and use the crosscorrelation imaging condition can be represented as



Similarly, the operator that maps an image to the receiver wavefield is



Each sample of the wavefields $\mathbf{B}_s$ and $\mathbf{B}_r$ represents the wavefield at one time step and at one spatial location. For elastic imaging, one sample contains multiple components of the wavefield, which can be represented by the imaging condition:



As mentioned earlier, quantities $\mathbf{B}_s$ and $\mathbf{B}_r$ are source and receiver wavefields in certain formats, depending on the imaging condition, As explained in the following sections.

2.1 Perturbation imaging condition

The α and β perturbation models can be derived using Born approximation (Hudson and Heritage, 1981; Jaramillo and Bleistein, 1999; Ribodetti et al., 2011). We consider the homogeneous elastic isotropic wave-equation:

$$\ddot{\mathbf{u}}_s - \alpha\nabla(\nabla\cdot\mathbf{u}_s) + \beta\nabla\times(\nabla\times\mathbf{u}_s) = \mathbf{d}_s\ , \tag{3}$$

where $\mathbf{u}_s\,(e,\mathbf{x},t) = [u_x\ \ u_y\ \ u_z]^T$ is the source displacement wavefield, which is a function of experiment e, space $\mathbf{x}$, and time t. Vector $\mathbf{d}_s\,(e,\mathbf{x},t)$ is the source function. The model $\mathbf{m}$ consists of two parameters $\alpha\,(\mathbf{x}) = \dfrac{\lambda+2\mu}{\rho}$ and $\beta\,(\mathbf{x}) = \dfrac{\mu}{\rho}$, which are squared P- and S-wave velocities, respectively. λ and μ are Lamé parameters, and ρ is the density.

Introducing the perturbation $\mathbf{m} = \begin{bmatrix} I^\alpha & I^\beta \end{bmatrix}^T$ to model $\mathbf{m}$ leads to the property model $\begin{bmatrix} \alpha + I^\alpha & \beta + I^\beta \end{bmatrix}^T$. The constructed wavefield is $\mathbf{u}_s + \delta\mathbf{u}_s$ computed using the same source term $\mathbf{d}_s$:

$$\begin{aligned} &(\ddot{\mathbf{u}}_s + \delta\ddot{\mathbf{u}}_s) \\ &-(\alpha + I^\alpha)\,\nabla[\nabla\cdot(\mathbf{u}_s+\delta\mathbf{u}_s)] \\ &+\left(\beta + I^\beta\right)\nabla\times[\nabla\times(\mathbf{u}_s+\delta\mathbf{u}_s)] \\ &=\mathbf{d}_s\ , \end{aligned} \tag{4}$$

where $\delta\mathbf{u}_s$ is the perturbed wavefield:

By ignoring the high order terms $I^\alpha\nabla(\nabla\cdot\delta\mathbf{u}_s)$ and $I^\beta\nabla\times(\nabla\times\delta\mathbf{u}_s)$, and subtracting equation 3 from equation 4, we obtain a relation for the perturbed wavefield $\delta\mathbf{u}_s$:

$$\begin{aligned} &\delta\ddot{\mathbf{u}}_s \\ &-\alpha\nabla(\nabla\cdot\delta\mathbf{u}_s) \\ &+\beta\nabla\times(\nabla\times\delta\mathbf{u}_s) \\ &=[\nabla(\nabla\cdot\mathbf{u}_s)\ \ -\nabla\times(\nabla\times\mathbf{u}_s)]\begin{bmatrix} I^\alpha \\ I^\beta \end{bmatrix}\ . \end{aligned} \tag{5}$$

Therefore, the format of the source wavefield $\mathbf{B}_{sP}$ at each time and space position is

$$\mathbf{B}_{sP} = [\nabla(\nabla\cdot\mathbf{u}_s)\ \ -\nabla\times(\nabla\times\mathbf{u}_s)]\ . \tag{6}$$

The predicted data are extracted from the perturbed wavefield $\delta\mathbf{u}_s$ at the receiver locations. Therefore, for the perturbation imaging condition the demigration operator used in equation 1 can be defined as

$$\mathbf{F} = \mathbf{KPB}_{sP}\ . \tag{7}$$

In operator $\mathbf{B}_{sP} = [\nabla(\nabla\cdot\mathbf{u}_s)\ \ -\nabla\times(\nabla\times\mathbf{u}_s)]$, the first and second components are the decomposed P- and S-modes in the source wavefield $\mathbf{u}_s$, respectively. Operator $\mathbf{P}$ is the elastic forward modeling, and it computes the perturbed wavefield $\delta\mathbf{u}_s$ using the source term $\mathbf{B}_{sP}\mathbf{m}$, and operator $\mathbf{K}$ restricts the perturbed wavefield $\delta\mathbf{u}_s$ to the known receiver positions. This process transforms model $\mathbf{m}$ to $\mathbf{d}_r$, and its adjoint operator

$$\mathbf{F}^{\mathsf{T}} = \mathbf{B}_{sP}^{\mathsf{T}}\mathbf{P}^{\mathsf{T}}\mathbf{K}^{\mathsf{T}}\ . \tag{8}$$

maps the recorded data $\mathbf{d}_r$ to image $\mathbf{m}$. Operator $\mathbf{K}^{\mathsf{T}}$ injects the recorded data $\mathbf{d}_r$ into the wavefield, and then the adjoint wave propagation operator $\mathbf{P}^{\mathsf{T}}$ computes the receiver displacement wavefield $\mathbf{u}_r$. The image $\mathbf{m}$ is computed by crosscorrelating the source wavefield $\mathbf{B}_{sP}$ and receiver wavefield $\mathbf{B}_{rP}$, which is displacement wavefield $\mathbf{u}_r$. Therefore, equation 8 indicates a perturbation imaging condition for elastic RTM:

$$I^\alpha = \sum_{e,t}\nabla(\nabla\cdot\mathbf{u}_s)\cdot\mathbf{u}_r, \tag{9}$$

$$I^\beta = \sum_{e,t} -\nabla\times(\nabla\times\mathbf{u}_s)\cdot\mathbf{u}_r\ . \tag{10}$$

2.2 Displacement imaging condition

The displacement image(Yan and Sava, 2008) is defined by crosscorrelating all combinations of components of the source and receiver displacement wavefields:

$$\mathbf{m} = [I^{xx}\ \ I^{xy}\ \ I^{xz}\ \ I^{yx}\ \ I^{yy}\ \ I^{yz}\ \ I^{zx}\ \ I^{zy}\ \ I^{zz}]^T\ , \tag{11}$$

where

$$I^{ij} = \sum_{e,t} u_{si}u_{rj}\ . \tag{12}$$

Quantities $u_i\,(e,\mathbf{x},t)$ and $u_j\,(e,\mathbf{x},t)$ ($i,j = x,y,z$) are the x- ,y-, and z-components of the source displacement wavefield $\mathbf{u}_s$ and receiver wavefield $\mathbf{u}_r$. In order to construct the migration operator, we define the receiver wavefield $\mathbf{B}_{sD}$ as the receiver displacement wavefield $\mathbf{u}_r$, and source wavefield $\mathbf{B}_{sD}$ for each time and space position as

$$\mathbf{B}_{sD} = \mathbf{E}\mathbf{u}_s\,[\mathbf{E}\ \ \mathbf{E}\ \ \mathbf{E}]\ , \tag{13}$$

where matrix $\mathbf{E}$ is a 3x3 identity matrix:

$$\mathbf{E} = \begin{bmatrix} 1 & 0 & 0 \\ 0 & 1 & 0 \\ 0 & 0 & 1 \end{bmatrix}\ . \tag{14}$$

Then, the migration operator mapping the recorded data $\mathbf{d}_r$ to the displacement image is

$$\mathbf{F}^{\mathsf{T}} = \mathbf{B}_{sD}^{\mathsf{T}}\mathbf{P}^{\mathsf{T}}\mathbf{K}^{\mathsf{T}}\ . \tag{15}$$

We construct the receiver wavefield $\mathbf{u}_r$ by applying the adjoint wave propagation operator $\mathbf{P}^\mathsf{T}$ to the wavefield $\mathbf{K}^\mathsf{T}\mathbf{d}_r$. The image $\mathbf{m}$ is computed by crosscorrelating the source wavefield $\mathbf{B}_{sD}$ and receiver wavefield $\mathbf{u}_r$. Thus, the demigration operator $\mathbf{F}$ is:

$$\mathbf{F} = \mathbf{KPB}_{sD} \ . \tag{16}$$

Operator $\mathbf{P}$ computes the perturbed wavefield $\delta\mathbf{u}_s$ using the source term $\mathbf{B}_{sD}\mathbf{m}$ and then operator $\mathbf{K}$ restricts the perturbed wavefield $\delta\mathbf{u}_s$ to the known receiver positions.

2.3 Potential imaging condition

The potential image (Yan and Sava, 2008) is defined as

$$\mathbf{m} = \begin{bmatrix} I^{PP} & \mathbf{I}^{PS} & \mathbf{I}^{SP} & I^{SS} \end{bmatrix}^T \ , \tag{17}$$

by crosscorrelating decomposed P and S wavefield with each P and S component of the receiver wavefield, where

$$I^{PP} = \sum_{e,t} P_s P_r \ , \tag{18}$$

$$\mathbf{I}^{PS} = \sum_{e,t} P_s \mathbf{S}_r \ , \tag{19}$$

$$\mathbf{I}^{SP} = \sum_{e,t} \mathbf{S}_s P_r \ , \tag{20}$$

$$I^{SS} = \sum_{e,t} \mathbf{S}_s \cdot \mathbf{S}_r \ . \tag{21}$$

For each time and space sample, the source wavefield $\mathbf{B}_{sJ}$ is of which the

$$\mathbf{B}_{sJ} = \begin{bmatrix} \nabla\cdot\mathbf{u}_s & \nabla\cdot\mathbf{u}_s & 0 & 0 \\ 0 & 0 & \nabla\times\mathbf{u}_s & \nabla\times\mathbf{u}_s \end{bmatrix} \ , \tag{22}$$

where the receiver wavefield $\mathbf{B}_{rJ}$ is obtained by applying Helmholtz decomposition to the receiver displacement wavefield $\mathbf{u}_r$:

$$\mathbf{B}_{rJ} = \mathbf{H}^\mathsf{T}\mathbf{u}_r \ . \tag{23}$$

The Helmholtz decomposition operator $\mathbf{H}^\mathsf{T}$ separates the displacement wavefield $\mathbf{u}_r$ into its P and S components:

$$\mathbf{H}^\mathsf{T} = \begin{bmatrix} \nabla\cdot \\ \nabla\times \end{bmatrix} \ . \tag{24}$$

This displacement imaging condition uses the migration operator $\mathbf{F}^\mathsf{T}$ that maps the recorded data $\mathbf{d}_r$ to the potential image $\mathbf{m}$:

$$\mathbf{F}^\mathsf{T} = \mathbf{B}_{sJ}^\mathsf{T}\mathbf{H}^\mathsf{T}\mathbf{P}^\mathsf{T}\mathbf{K}^\mathsf{T} \ . \tag{25}$$

The demigration operator $\mathbf{F}$ can be obtained using the adjoint operators:

$$\mathbf{F} = \mathbf{KPHB}_{sJ} \ . \tag{26}$$

The source term for Born modeling is $\mathbf{HB}_{sJ}\mathbf{m}$, where operator $\mathbf{H}$ computes displacement wavefield using the decomposed P and S components $\mathbf{B}_{sJ}\mathbf{m}$. Operator $\mathbf{P}$ computes the perturbed wavefield $\delta\mathbf{u}_s$ using the source term $\mathbf{HB}_{sJ}\mathbf{m}$ and operator $\mathbf{K}$ restricts the perturbed wavefield $\delta\mathbf{u}_s$ to the known receiver positions.

2.4 Scalar imaging condition

The scalar image (Duan and Sava, 2015) is defined as

$$\mathbf{m} = \begin{bmatrix} I^{PP} & I^{PS} & I^{SP} & I^{SS} \end{bmatrix}^T \ , \tag{27}$$

with scalar images

$$I^{PP} = \sum_{e,t} P_s P_r \ , \tag{28}$$

$$I^{PS} = \sum_{e,t} (\nabla P_s \times \mathbf{n}) \cdot \mathbf{S}_r \ , \tag{29}$$

$$I^{SP} = \sum_{e,t} ((\nabla \times \mathbf{S}_s) \cdot \mathbf{n}) \, P_r \ , \tag{30}$$

$$I^{SS} = \sum_{e,t} \mathbf{S}_s \cdot \mathbf{S}_r \ , \tag{31}$$

where vector $\mathbf{n}(\mathbf{x})$ denote the local normal vector to the locally-planar interface.

This imaging condition is derived by exploiting pure P- and S-modes obtained by Helmholtz decomposition. Similar to the LSM algorithm using the scalar imaging condition, we decompose the receiver displacement wavefield $\mathbf{u}_r$ to P- and S-modes using Helmholtz decomposition and crosscorrelate the source wavefield $\mathbf{B}_{sY}$ and receiver wavefield $\mathbf{B}_{rY}$ to compute the image $\mathbf{m}$.

Wavefield $\mathbf{B}_{sY}$ contains the source displacement wavefield $\mathbf{u}_s$ and reflector normal $\mathbf{n}$. The source wavefield at each time and space sample is

$$\mathbf{B}_{sY} = \begin{bmatrix} \nabla\cdot\mathbf{u}_s & \nabla(\nabla\cdot\mathbf{u}_s)\times\mathbf{n} & 0 & 0 \\ 0 & 0 & \nabla\times(\nabla\times\mathbf{u}_s)\cdot\mathbf{n} & \nabla\times\mathbf{u}_s \end{bmatrix} \ . \tag{32}$$

The migration operator $\mathbf{F}^\mathsf{T}$ is

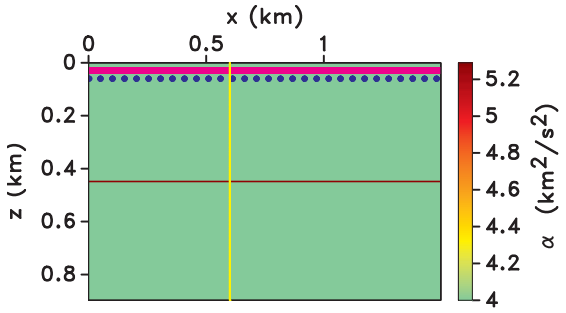
$$\mathbf{F}^\mathsf{T} = \mathbf{B}_{sY}^\mathsf{T}\mathbf{H}^\mathsf{T}\mathbf{P}^\mathsf{T}\mathbf{K}^\mathsf{T} \ , \tag{33}$$

and the demigration operator $\mathbf{F}$ can be obtained using the adjoint of the sequential operators contained in equation 33:

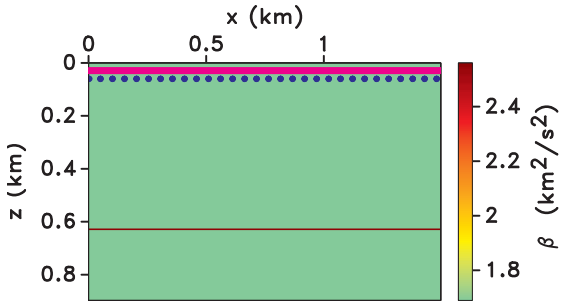
$$\mathbf{F} = \mathbf{KPHB}_{sY} \ . \tag{34}$$

The source term for Born modeling is $\mathbf{HB}_{sY}\mathbf{m}$, where operator $\mathbf{H}$ computes displacement wavefield using the P and S components $\mathbf{B}_{sY}\mathbf{m}$.

Among the four proposed LSRTM images, only the perturbation image and scalar image do not change polarity, and they can be stacked over experiments without an additional correction. Although the value of each component of the scalar image is related to reflectivity, the physical interpretation of the perturbation image is more straightforward, as the two components of the image are simply perturbations of the squared P and S velocities. In addition, the perturbation imaging condition does not require additional information about the subsurface, such as the geologic dip.



(a)



(b)

Figure 1. (a) α model with a horizontal reflector at $z = 0.45$ km, and (b) β model with a horizontal reflector at $z = 0.62$ km. The line at $z = 0.03$ km shows the receiver positions, and the dots denote the location of the sources, at $z = 0.06$ km.

3 EXAMPLES

3.1 Layered model

We use a simple example to demonstrate the algorithms for elastic migration. Each of the α and β models contains one horizontal reflector, but the two reflectors are at different depths, as shown in Figures 1(a) and 1(b). We generate 30 two-component shot gathers using a vertical displacement source with a 30Hz peak frequency Ricker wavelet. Figures 2(a)–2(f) show the x- and z-component snapshots of a wavefield with the source at $\{0.76, 0.06\}$ km. The P wave generates reflections at the reflector in the α model, but not at the reflector in the β model. Similarly, The S wave generates reflections at the reflector in the β model, but not at the reflector in the α model. We also observe internal multiples that bounce between the two reflectors. The x- and z-components of this shot gather after direct wave removal are shown in Figures 3(a) and 3(b), respectively. Note that four strong arrivals which are, from top to bottom, PP, PS, SP, and SS reflections. Using the perturbation imaging condition (equation 7), we obtain the perturbation images for α and β shown in Figures 4(a) and 4(b), respectively. Notice that additional reflectors appear in both α and β perturbation images, and these reflectors are generated by fake modes in the constructed receiver wavefield.

Figures 4(c) and 4(d) are the LSRTM images after 10 iterations. Compared to the RTM images (Figures 4(a) and 4(b)), the artifacts in the LSRTM images are attenuated. Moreover, comparing the amplitudes of the computed images with the true model at $x = 0.6$ km, we notice that peak values of the LSRTM images are closer to the amplitudes of the true perturbation than the values of the RTM images. Therefore, LSRTM improves elastic imaging with true amplitude information and fewer artifacts, including artifacts caused by the nonphysical modes.

3.2 Marmousi model

The Marmousi-II model (Martin et al., 2006) is full elastic, that supports not only compressional waves, but also shear waves, and converted waves. The model contains hydrocarbon units, which dramatically decrease the value of α , but slightly increase the value of β. Therefore, the true α and β are inconsistent in areas with hydrocarbon units in various sizes, which is challenging to elastic LSRTM.

We model 40 shots evenly spaced on the surface using a displacement source with a 30Hz peak frequency Ricker wavelet. The horizontal and vertical components of the source function have the same amplitude. The receiver spread is fixed for all shots and spans from 0 to 3.0 km with a 0.005 km sampling. Figures 6(a) and 6(b) show the background model for α and β, respectively, and they both contain a homogeneous layer on the top. The recorded data are modeled according to equation 8. Figures 7(a) and 7(b) show the corresponding true perturbation model for α and β, respectively. The perturbation models are not identical, e.g., only the α model shows a reflector with negative value at $\{2, 0.4\}$ km.

The z-component of one shot gather with the source location at $\{1.54, 0.013\}$ km is shown in Figure 8(a). The arrival with high amplitude is the reflection from the bottom of the homogeneous layer, and its amplitude is much stronger than other arrivals in the recorded data. Thus this arrival generates strong artifacts in the computed image and the inversion mostly focuses on generating a image that best match this strong arrivals, instead of the late arrivals with weaker amplitudes. In order to obtain a more uniform update using all arrivals, we use the data weighting term $\mathbf{W}$ to down-weight the arrivals with strong amplitudes. We calculate an envelope around the strong arrivals in the recorded data, and define the data weighting function by assigning a small value to the strong arrival envelope. We also apply a smoothing operator in the data space to the weighting function to avoid discontinuity along time and space axises. Figure 8(b) shows the weighting function in the data domain, which we compute from the shot gather Figure 8(a). Figures 9(a) and 9(b) are the x- and z-components of the down-weighted shot gather, respectively. Compared to the original recorded data (Figure 8(a)), the amplitudes of the arrivals in the down-weighted data (Figure 9(b)) are more balanced.

The LSRTM images after 112 iterations are shown in Figures 10(a) and 10(b). The update image for α has higher resolution than β because, in general, S waves have shorter wavelengths than P waves, and we do not consider attenuation in this experiment. The updated images are consistent

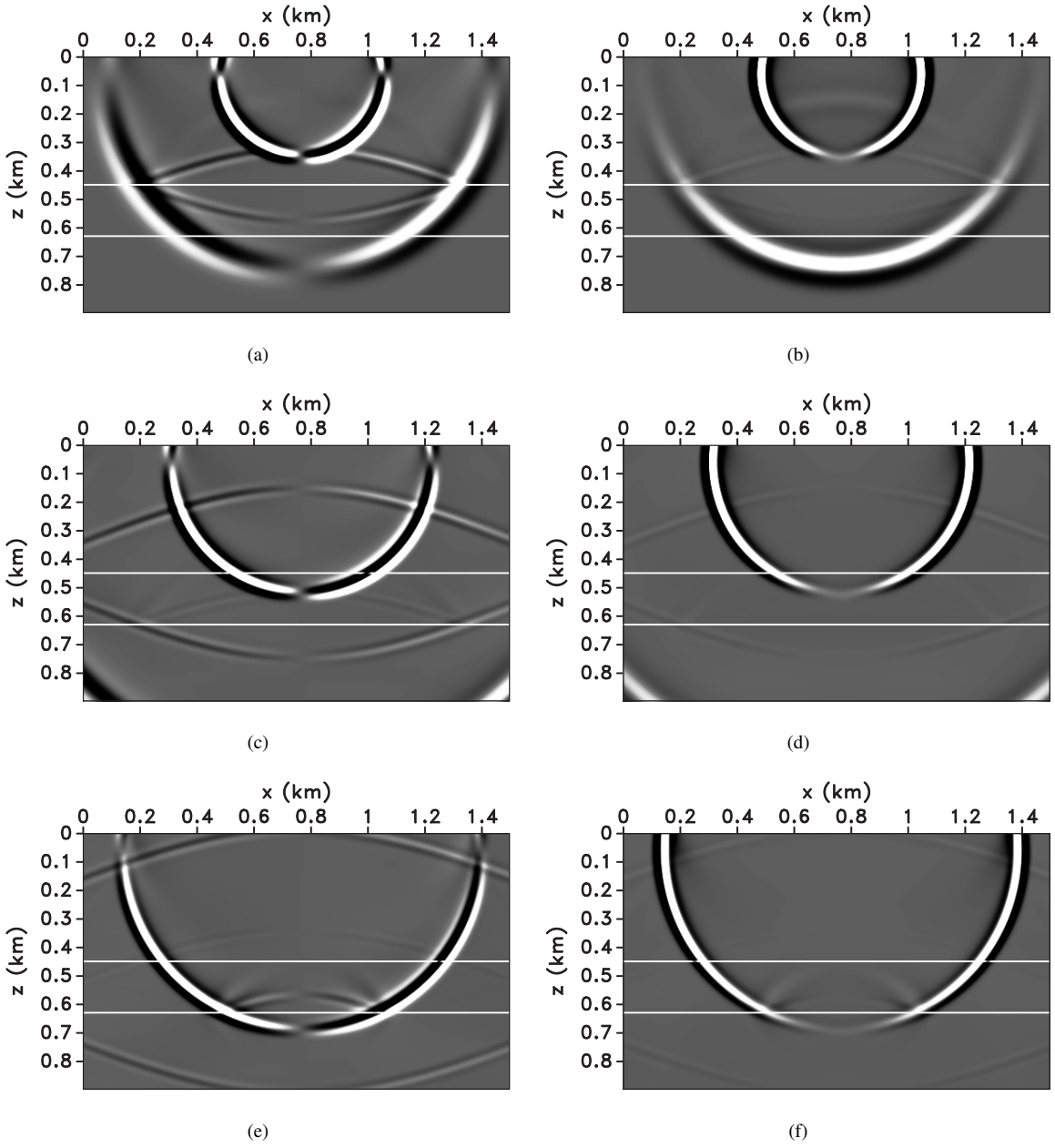


Figure 2. Snapshots of an elastic wavefield, for a source is at coordinates $\{0.76, 0.06\}$ km. (a) X- and (b) z-components of the wavefield at $t = 0.2$ s; (c) x- and (d) z-components of the wavefield at $t = 0.3$ s; (e) x- and (f) z-components of the wavefield at $t = 0.4$ s. Two white lines indicate the locations of reflectors in α and β models. P waves generate reflections only at the top reflector; S waves generate reflections only at the bottom reflector;

with the true perturbation images. For example, only the α image (Figure 10(a)) contains the reflector with negative value at $\{2, 0.4\}$ km, which corresponds to a hydrocarbon unit in the true model that only decreases the value of α.

Figures 11(a) and 11(b) show the x- and z-components of the predicted shot gather, respectively, using the updated images (Figures 10(a) and 10(b)). The same weighting functions are applied to the two gathers. For most arrivals, the predicted data match the recorded data in both phase and amplitude. Figures 12(a) and 12(b) compare traces from the inverted α and β images at $x = 1.5$ km with the true perturbation models. The amplitudes of the inverted images match the true perturbation models well.

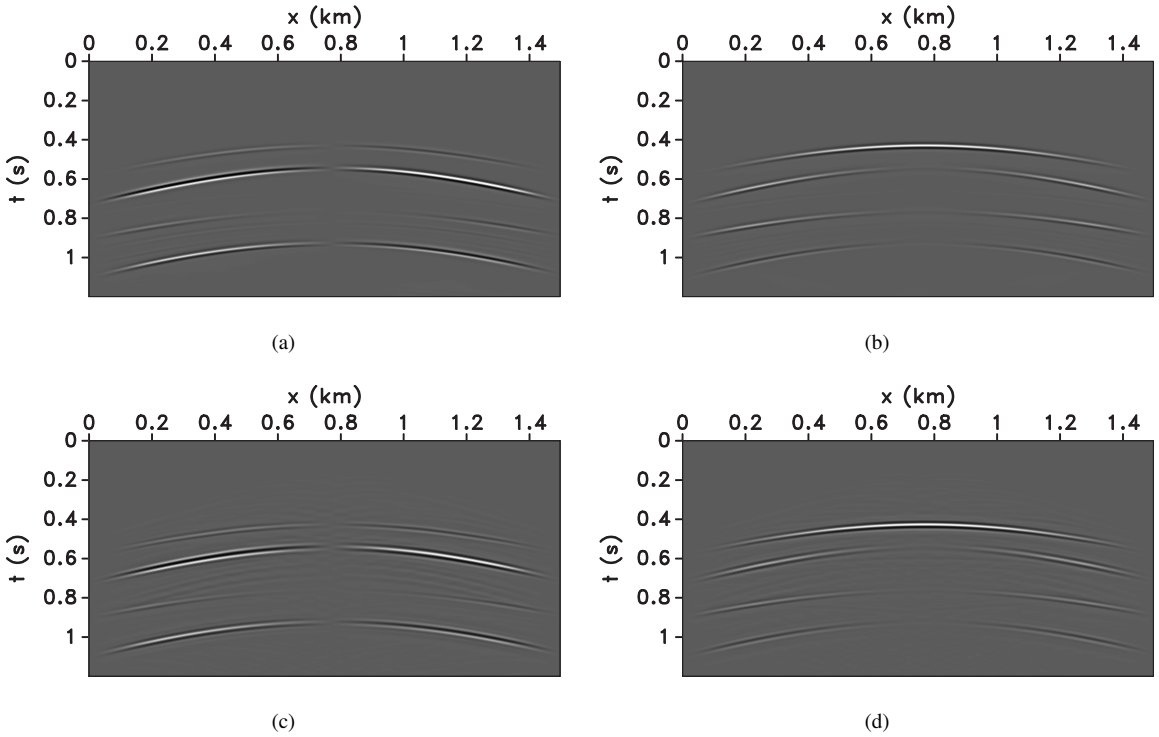


Figure 3. (a) X- and (b) z-components of the recorded data for a source at $\{0.76, 0.06\}$ km. (c) x- and (d) z-components of the predicted data using the inverted model. The direct arrivals are removed in the shot gathers. Note that the predicted data match the recorded data in both phase and amplitude.

4 CONCLUSIONS

We propose methods for elastic least-squares reverse time migration based on four imaging conditions: a perturbation imaging condition, displacement imaging condition, potential imaging condition, and scalar imaging condition. Among these, only the perturbation and scalar imaging conditions yield images that do not suffer from polarity changes, and thus can be stacked over experiments without additional image corrections. Numerical tests of the perturbation imaging condition demonstrate that elastic LSRTM produces images with fewer migration artifacts and higher resolution compared to the corresponding RTM image. Compared to RTM, however, LSRTM has higher computational cost, and more work is needed to improve the convergence rate. Nevertheless, elastic LSRTM provides true-amplitude perturbations and high-resolution images, which makes the algorithm especially suitable for certain key applications such as reservoir charaterization.

5 ACKNOWLEDGMENTS

We thank the sponsors of the Center for Wave Phenomena, whose support made this research possible. The reproducible numeric examples in this paper use the Madagascar open-source software package (Fomel et al., 2013) freely available from http://www.ahay.org.

REFERENCES

Artman, B., I. Podladtchikov, and A. Goertz, 2009, Elastic time-reverse modeling imaging conditions: SEG Technical Program Expanded Abstracts 2009, 1207–1211.

Claerbout, J. F., 1992, Earth soundings analysis: Processing versus inversion: Blackwell Scientific Publications Cambridge, Massachusetts, USA, **6**.

Dai, W., and G. T. Schuster, 2013, Plane-wave least-squares reverse-time migration: Geophysics, **78**, S165–S177.

Dai, W., X. Wang, and G. T. Schuster, 2011, Least-squares migration of multisource data with a deblurring filter: Geophysics, **76**, R135–R146.

Denli, H., and L. Huang, 2008, Elastic-wave reverse-time migration with a wavefield-separation imaging condition: SEG Technical Program Expanded Abstracts 2008, 2346–2350.

Dong, S., J. Cai, M. Guo, S. Suh, Z. Zhang, B. Wang, and Z. Li, 2012, Least-squares reverse time migration: towards true amplitude imaging and improving the resolution: Presented at the 2012 SEG Annual Meeting, Society of Exploration Geophysicists.

Du, Q., Y. Zhu, and J. Ba, 2012, Polarity reversal correction for elastic reverse time migration: Geophysics, **77(2)**, S31–S41.

Duan, Y., and P. Sava, 2014, Elastic reverse-time migration with obs multiples: Presented at the 2014 SEG Annual Meeting, Society of Exploration Geophysicists.

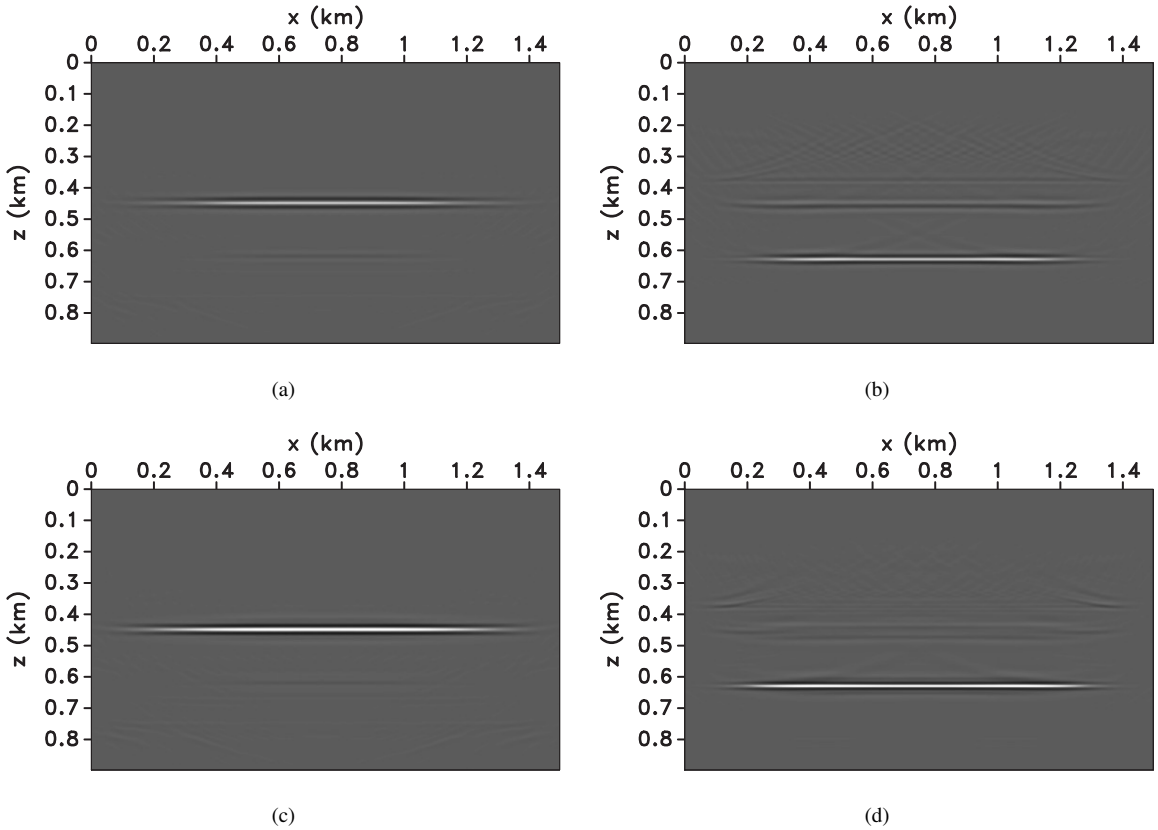


Figure 4. (a) α and (b) β perturbation images after first iteration. In addition to the event at the correct depth, there are two strong horizontal events in the β image, which are artifacts. (c) α and (d) β perturbation images after 10 iterations. Compare to the α and β images after the first iteration, the artifacts have been attenuated.

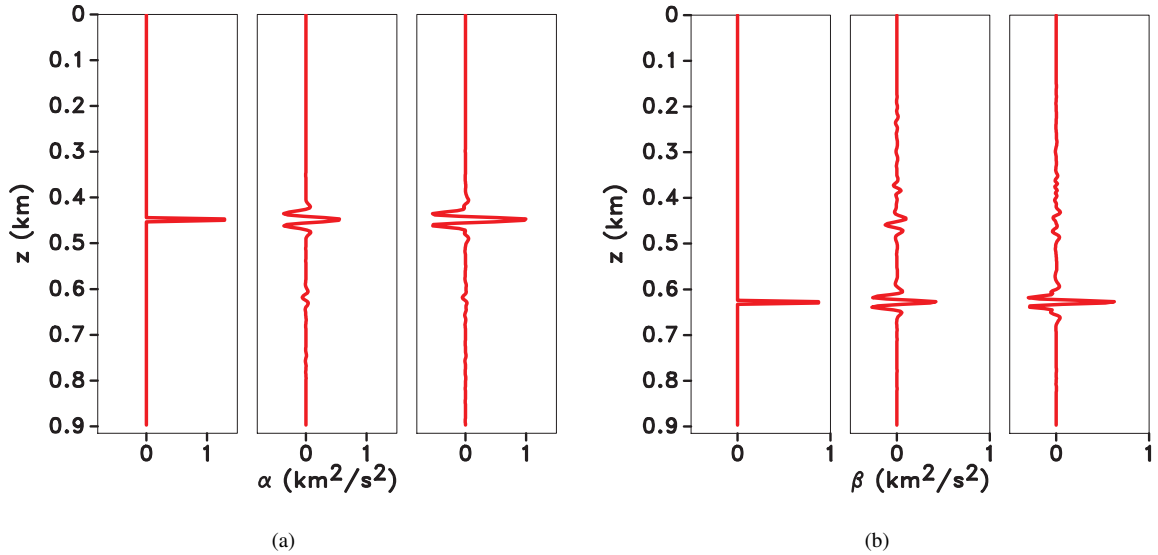
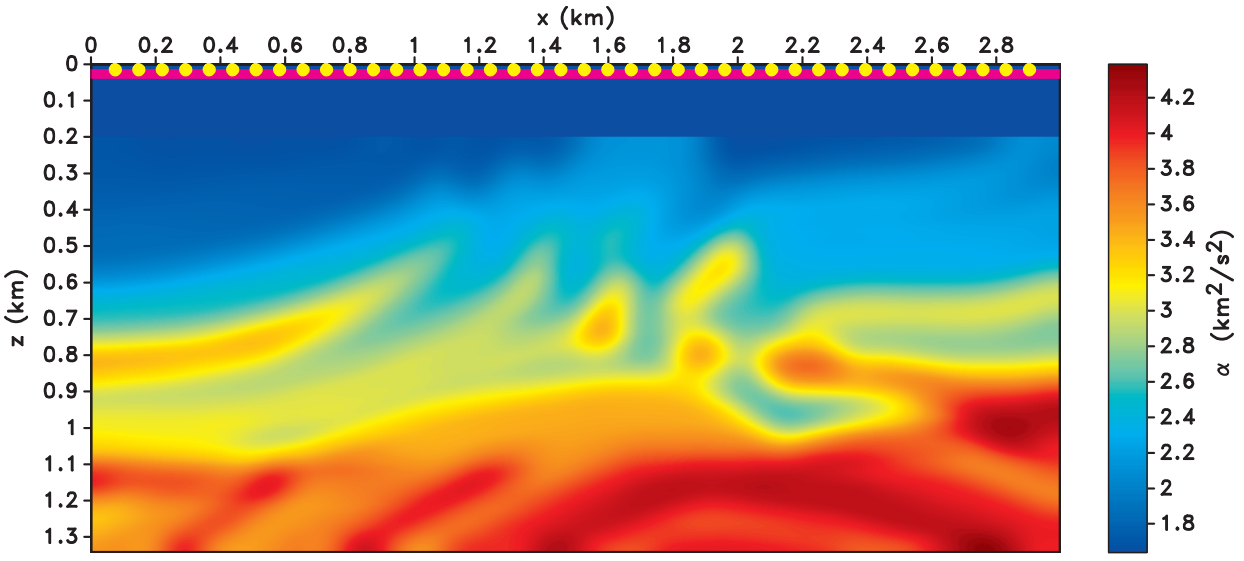
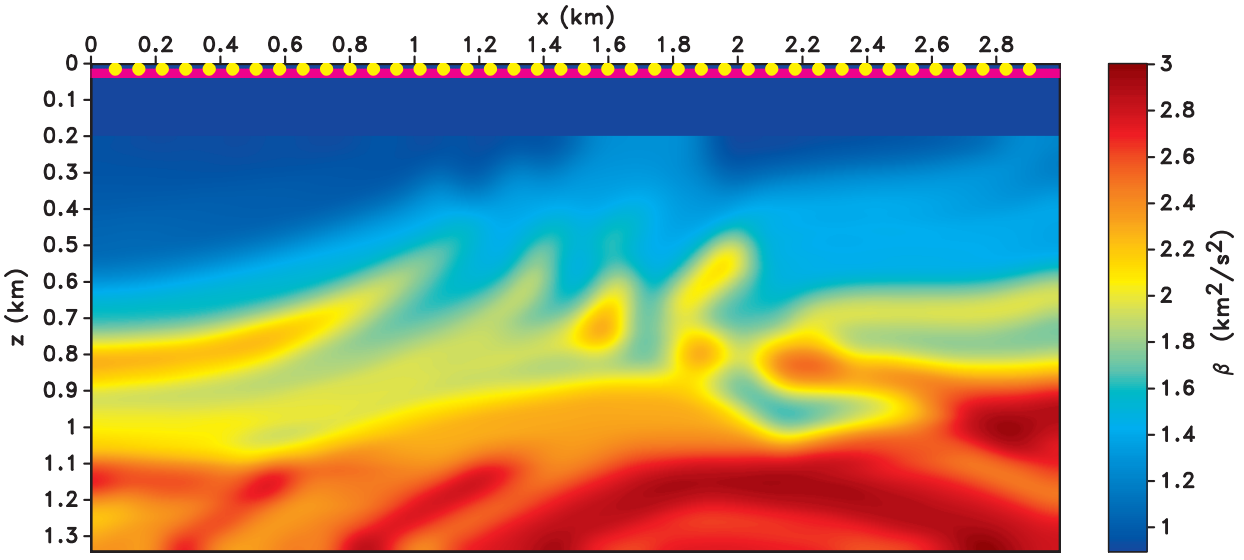


Figure 5. (a) Traces extracted from the true model perturbation, the RTM image, and the inverted model for α at $x = 0.6$ km. (b) Traces extracted from the true model perturbation, the RTM image, and the inverted model for β at $x = 0.6$ km. Note that peak values of the LSM images are closer to the amplitudes of the true perturbation than the values of the RTM images.



(a)



(b)

Figure 6. Background (a) α and (b) β models for Marmousi example. The line at $z = 0.025$ km represents the receivers, and the dots at $z = 0.013$ km denote the locations of the sources. The top layer is homogenous for both background models.

———, 2015, Scalar imaging condition for elastic reverse time migration: Geophysics, **80**, S127–S136.

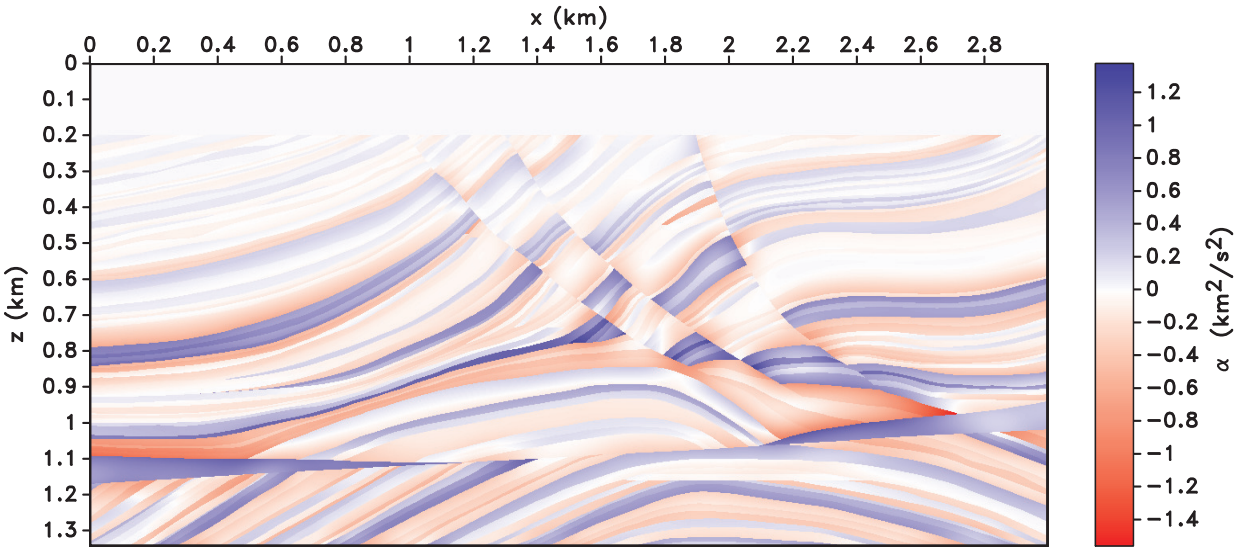
Fomel, S., P. Sava, I. Vlad, Y. Liu, and V. Bashkardin, 2013, Madagascar: open-source software project for multidimensional data analysis and reproducible computational experiments: Journal of Open Research Software, **1**, e8.

Huang, Y., and G. T. Schuster, 2012, Multisource least-squares migration of marine streamer and land data with frequency-division encoding: Geophysical Prospecting, **60**, 663–680.

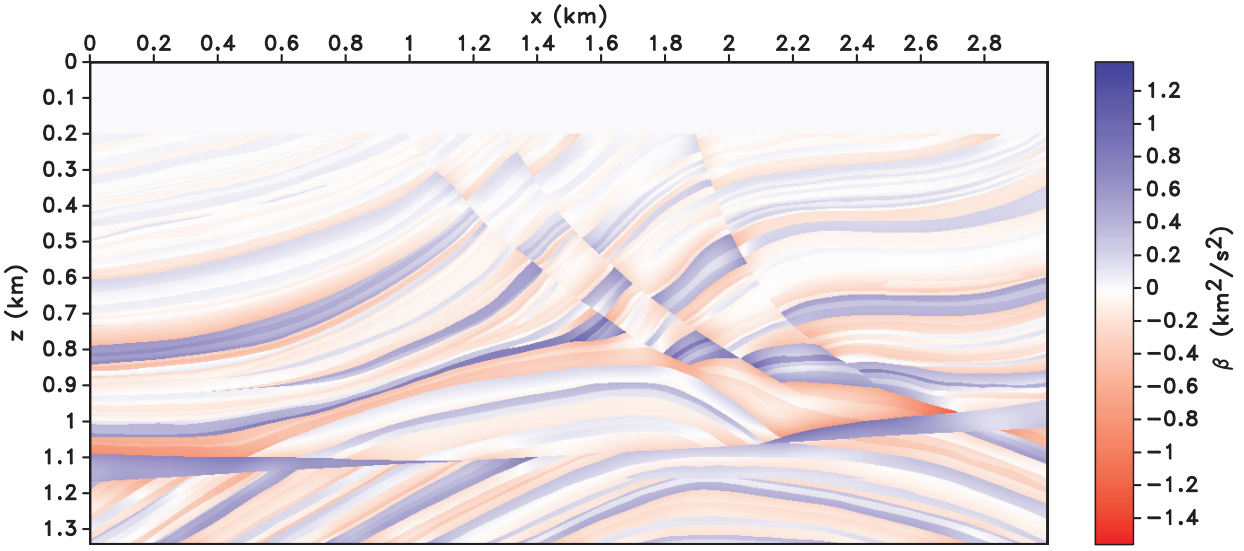
Hudson, J., and J. Heritage, 1981, The use of the Born approximation in seismic scattering problems: Geophysical Journal International, **66**, 221–240.

Jaramillo, H. H., and N. Bleistein, 1999, The link of Kirchhoff migration and demigration to Kirchhoff and Born modeling: Geophysics, **64**, 1793–1805.

Kaplan, S. T., P. S. Routh, and M. D. Sacchi, 2010, Derivation of forward and adjoint operators for least-squares shot-



(a)



(b)

Figure 7. True (a) α and (b) β perturbation models. The perturbation models are not identical, e.g., a reflector with negative value at $\{2, 0.4\}$ km is only in the α model.

profile split-step migration: Geophysics, **75**, S225–S235.

Kuehl, H., and M. Sacchi, 2002, Robust AVP estimation using least-squares wave-equation migration: Presented at the 2002 SEG Annual Meeting, Society of Exploration Geophysicists.

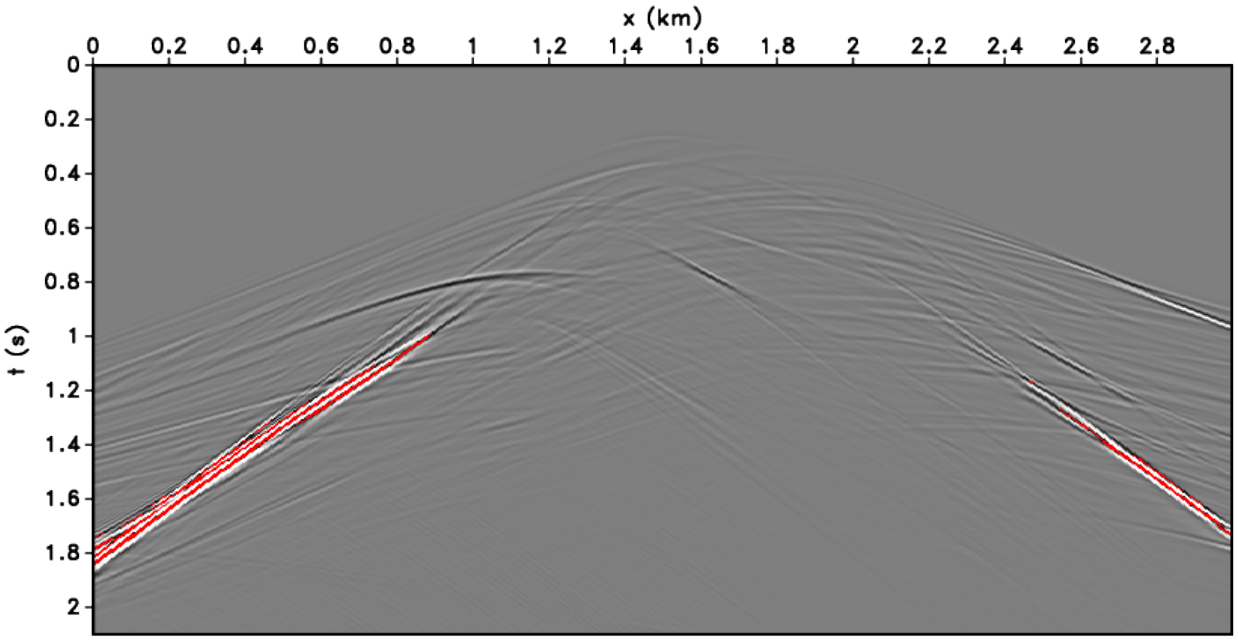
Luo, S., and D. Hale, 2014, Least-squares migration in the presence of velocity errors: Geophysics, **79**, S153–S161.

Martin, G. S., R. Wiley, and K. J. Marfurt, 2006, Marmousi2: An elastic upgrade for Marmousi: The Leading Edge, **25**, 156–166.

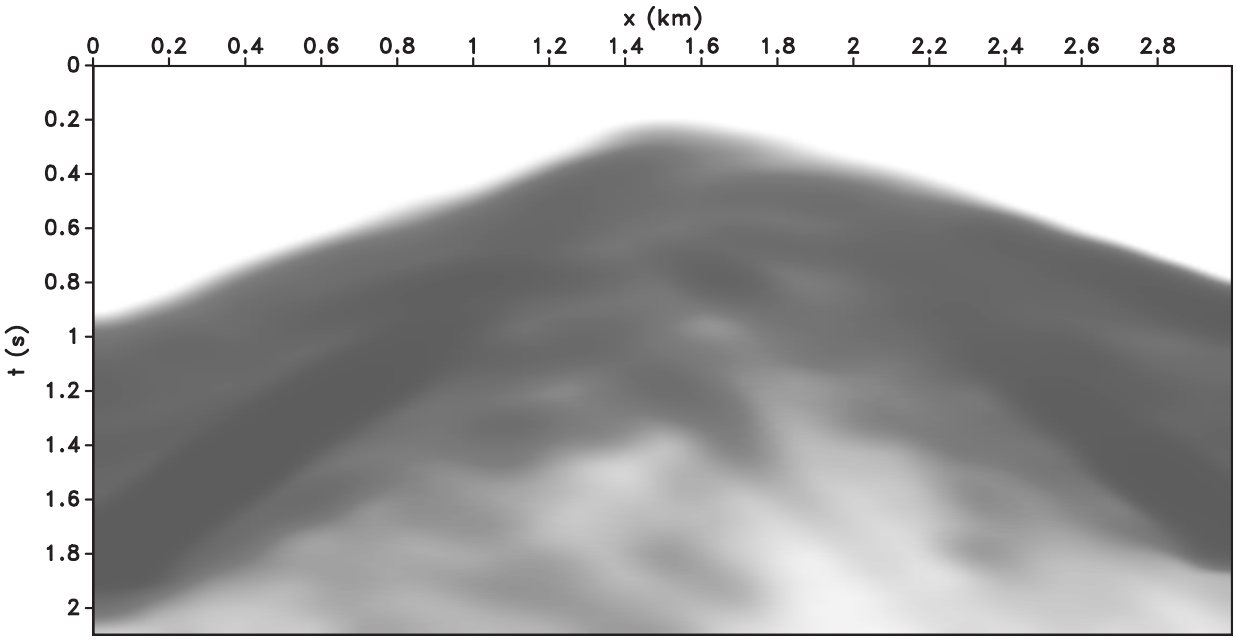
Nemeth, T., C. Wu, and G. T. Schuster, 1999, Least-squares migration of incomplete reflection data: Geophysics, **64**, 208–221.

Ribodetti, A., S. Operto, W. Agudelo, J.-Y. Collot, and J. Virieux, 2011, Joint ray+ Born least-squares migration and simulated annealing optimization for target-oriented quantitative seismic imaging: Geophysics, **76**, R23–R42.

Rocha, D., N. Tanushev, P. Sava, et al., 2015, Elastic wavefield imaging using the energy norm: Presented at the 2015 SEG Annual Meeting, Society of Exploration Geophysi-

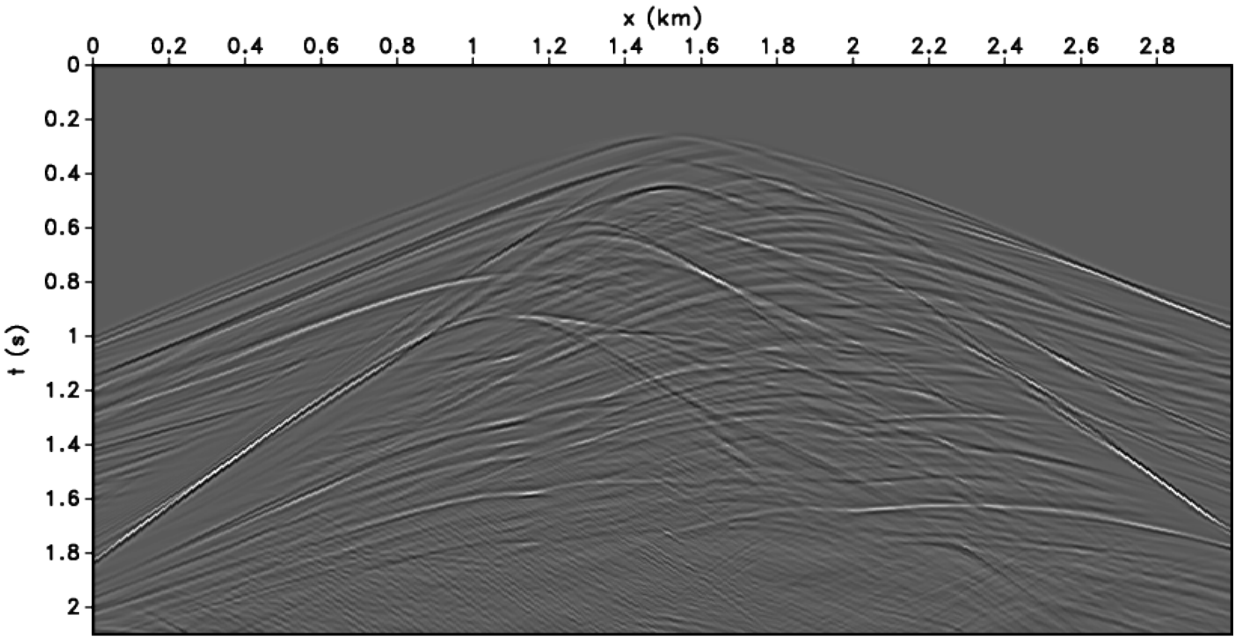


(a)

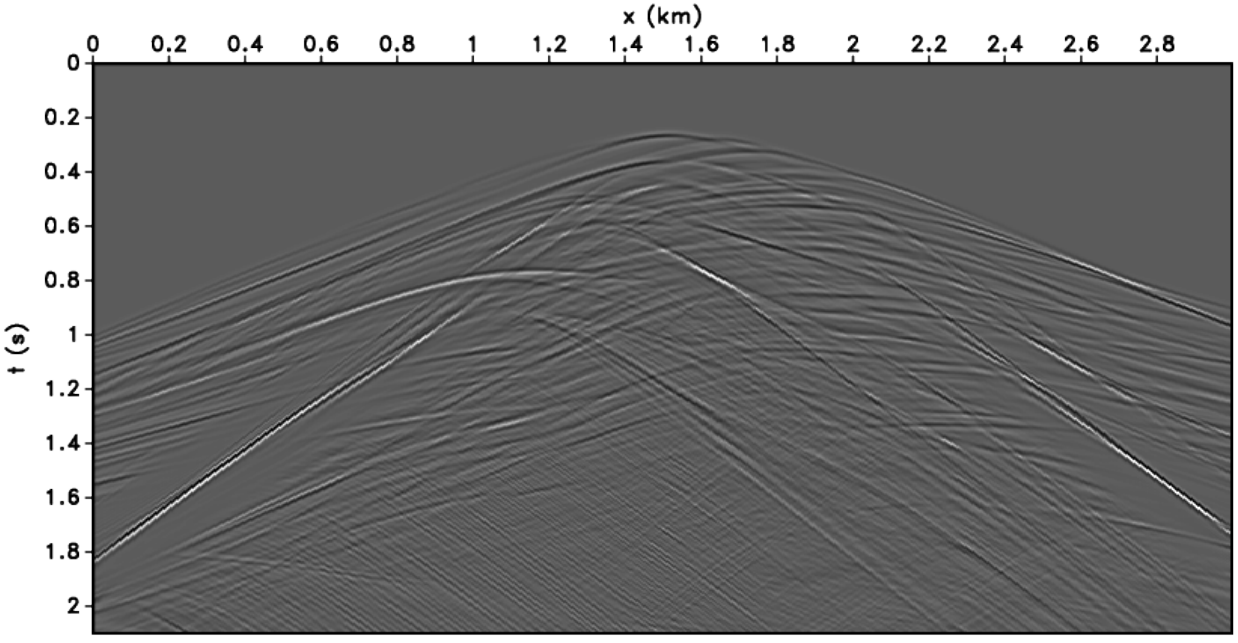


(b)

Figure 8. (a) Z-component of one shot gather with the source location at $\{1.54, 0.013\}$ km. The arrival with high amplitude is the reflection from the bottom of the homogeneous layer, and its amplitude is much stronger than other arrivals in the recorded data. (b) The data weighting function generated from the recorded data.



(a)



(b)

Figure 9. (a) X- and (b) z-components of the down-weighted shot gather. Note that the amplitudes of all arrivals are more balanced.

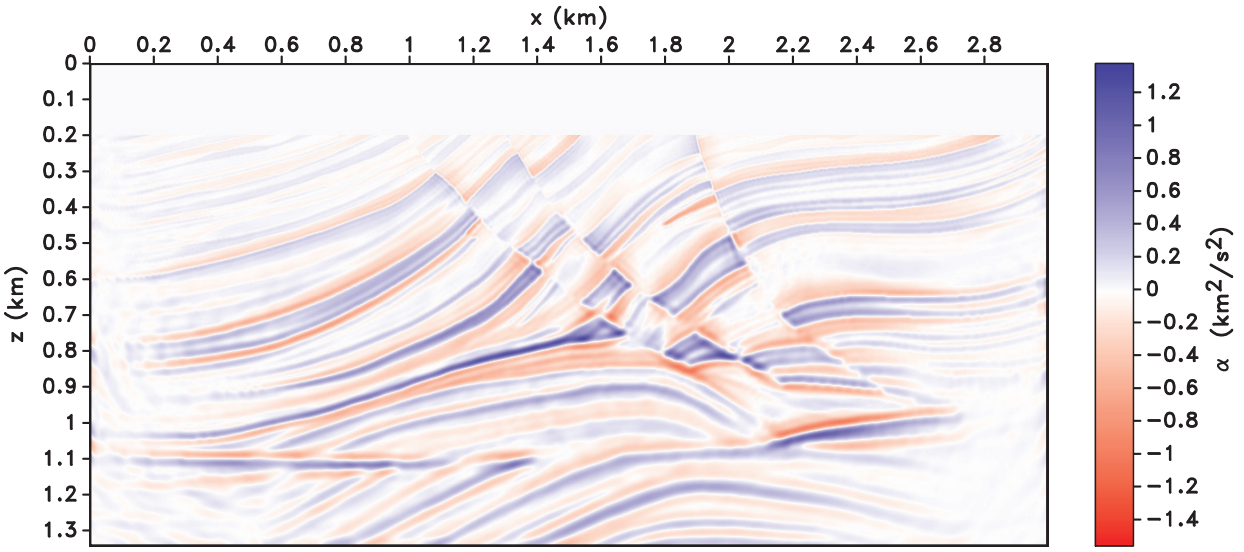
cists.

Schuster, G. T., 1993, Least-squares cross-well migration: SEG Technical Program Expanded Abstracts, 110–113.

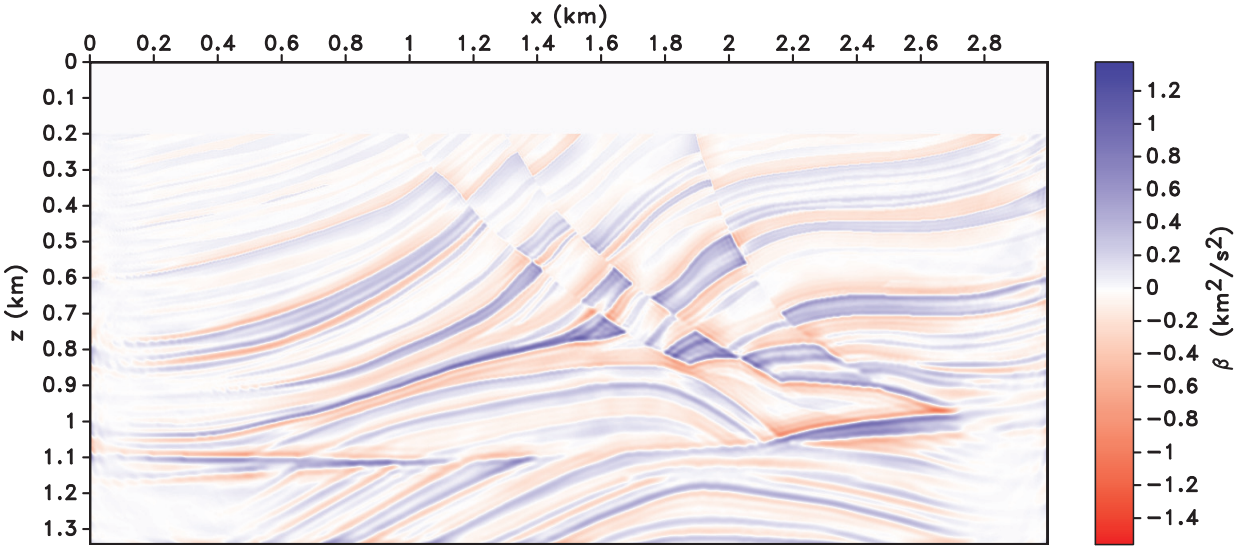
Stanton, A., and M. Sacchi, 2015, Least squares wave equation migration of elastic data: Presented at the 77th EAGE Conference and Exhibition 2015.

Sun, R., G. A. McMechan, C. Lee, J. Chow, and C. Chen, 2006, Prestack scalar reverse-time depth migration of 3D elastic seismic data: Geophysics, **71(5)**, S199–S207.

Trad, D., 2015, Least squares Kirchhoff depth migration: im-



(a)



(b)

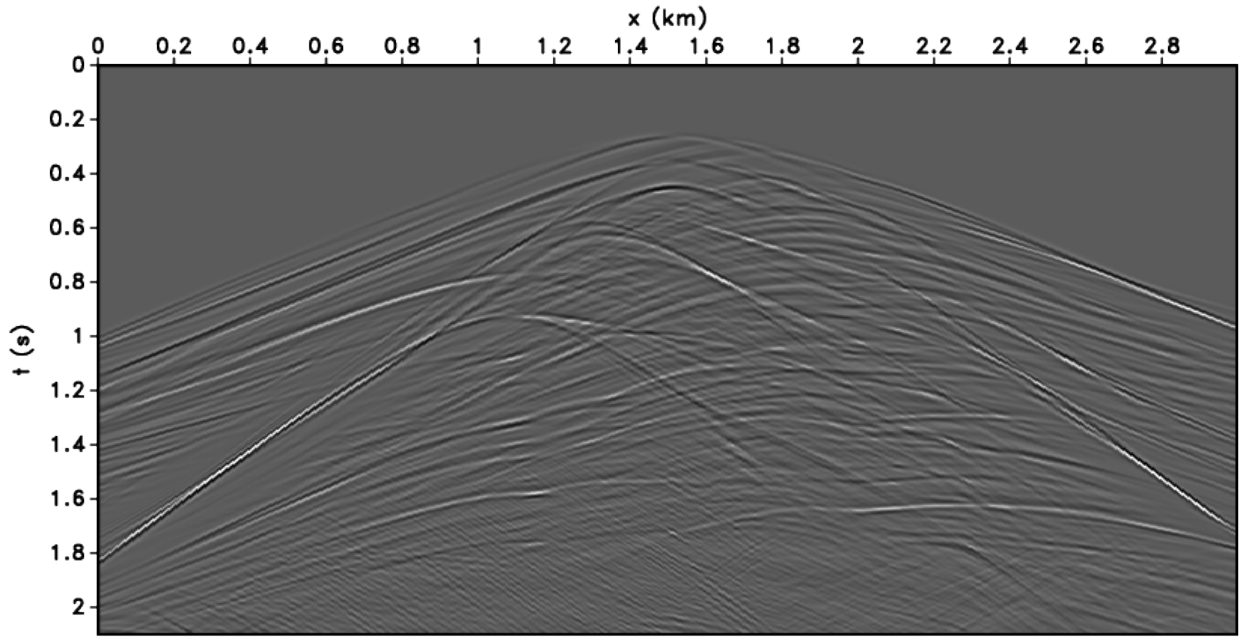
Figure 10. Updated (a) α and (b) β images after 112 iterations. Note that the updated images are consistent with the correponding true perturbation images. For example, we observe reflectors in the updated α image, but not in the updated β image.

plementation, challenges, and opportunities: Presented at the 2015 SEG Annual Meeting, Society of Exploration Geophysicists.

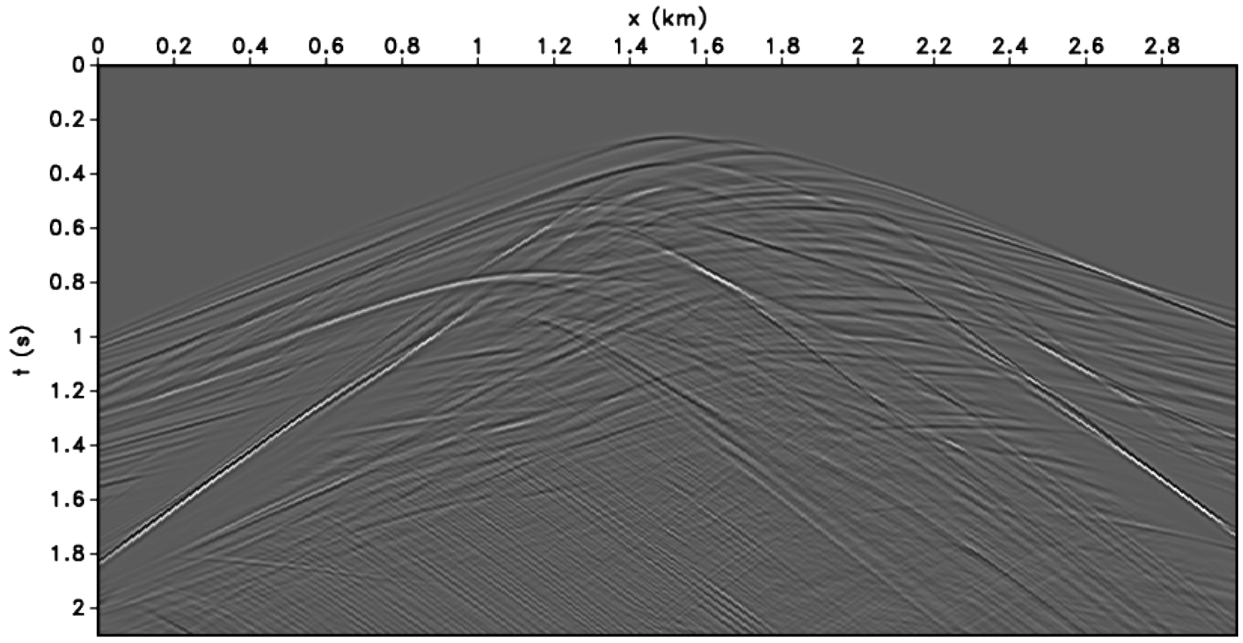
Wong, M., B. L. Biondi, and S. Ronen, 2015, Imaging with primaries and free-surface multiples by joint least-squares reverse time migration: Geophysics, **80**, S223–S235.

Wu, R., R. Yan, and X, 2010, Elastic converted-wave path migration for subsalt imaging: SEG Technical Program Expanded Abstracts 2010, 3176–3180.

Yan, J., and P. Sava, 2008, Isotropic angle-domain elastic reverse-time migration: Geophysics, **73(6)**, S229–S239.

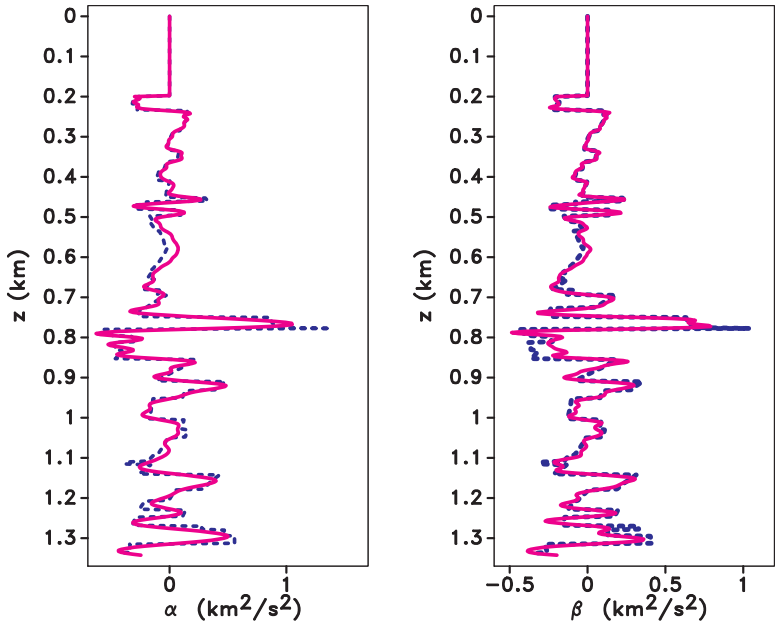


(a)



(b)

Figure 11. (a) X- and (b) z-components of the predicted shot gather using the updated models (Figures 10(a) and 10(b)). The same weighting functions (Figure 8(b)) are applied to the two gathers.



(a) (b)

Figure 12. Comparion between inverted images (solid lines) and true perturbation models (dashed lines) for (a) α and (b) β models. The traces are extracted at $x = 1.5$ km.